Coherent Interaction of a Few-Electron Quantum Dot with a Terahertz Optical Resonator

Kazuyuki Kuroyama, Jinkwan Kwoen, Yasuhiko Arakawa, and Kazuhiko Hirakawa

Phys. Rev. Lett. **132**, 066901 — Published 9 February 2024

DOI: 10.1103/PhysRevLett.132.066901

Coherent interaction of a-few-electron quantum dot with a terahertz optical resonator

Kazuyuki Kuroyama,[1,*] Jinkwan Kwoen,[2] Yasuhiko Arakawa,[2] and Kazuhiko Hirakawa[1,2,†]

[1] *Institute of Industrial Science, The University of Tokyo, 4-6-1 Komaba, Meguro-ku, Tokyo 153-8505, Japan*

[2] *Institute for Nano Quantum Information Electronics, The University of Tokyo, 4-6-1 Komaba, Meguro-ku, Tokyo 153-8505, Japan*

We have investigated light-matter hybrid excitations in a quantum dot (QD)-terahertz (THz) resonator coupled system. We fabricate a gate-defined QD near a THz split-ring resonator (SRR) by using a AlGaAs/GaAs two-dimensional electron system (2DES). By illuminating the system with THz radiation, the QD shows a current change whose spectrum exhibits coherent coupling between the electrons in the QD and the SRR as well as coupling between the 2DES and the SRR. The latter coupling enters the ultrastrong coupling regime and the electron excitation in the QD also exhibits coherent coupling with the SRR with the remarkably large coupling constant, despite the fact that only a few electrons reside in the QD.

Manipulation of charges and spins of electrons confined in quantum dots (QDs) is the core of semiconductor qubits [1–3]. For quantum information processing and multiplexing of qubits, it is highly desired to develop a technology of converting quantum information of electrons in the QDs to that of electromagnetic waves [4–6] and vice versa. To realize such quantum light-matter hybrid conversion, coherent coupling between electrons in QDs and electromagnetic waves in optical resonators has been proposed in the context of circuit quantum electrodynamics. Such coherent coupling between QDs and electromagnetic waves has so far been realized only for visible and microwave frequency ranges [7–15].

In order to improve the coupling strength of the electric-dipole interaction between an electron and a resonator, it is beneficial to reduce the mode volume of the resonator. It was shown that subwavelength metamaterial resonators in the terahertz (THz) frequency range can realize coherent coupling with two-dimensional (2D) electrons in semiconductor heterostructures with a large coupling strength [16–23]. Furthermore, exploiting a small mode volume of the subwavelength optical resonator, Valmora et al. realized deep strong coupling between a carbon nanotube QD and a THz optical resonator and observed novel resonator-induced conductance suppression [24].

In these previous studies, ultrastrong coupling of 2D electrons was often detected by performing THz optical transmission measurements on large-area metamaterial resonator arrays and, therefore, the read out of the coupling state of single QD-THz resonator systems has been technically very challenging, the device structures reported so far were rather complex or they were not very suitable for integration to large systems. Realization of hybrid quantum systems of a simpler structure by using top-down lithography approach is, therefore, highly desired.

In this work, we have fabricated a gate-defined QD in the vicinity of a gap of a THz split-ring resonator (SRR) placed on a 2D electron system (2DES) in semiconductor heterostructures and investigated interactions between electrons and a THz light field generated near the gap region of the SRR. We measured THz-induced photocurrent through the QD under a magnetic field, B. Excitations of electrons in the QD as well as 2D electrons respectively exhibited remarkably large anticrossing around the SRR resonance frequency. The obtained energy dispersion of the coupled system can be understood in terms of coupling between the 2D electrons and the SRR and that between the electrons in the QD and the SRR. The ratio of the Rabi frequency for the 2DES-SRR coupling to the SRR resonance frequency is found to be about 0.1, indicating that the system enters the ultrastrong coupling regime. Furthermore, the coupling strength between the QD and the SRR is also found to be close to that of the 2DES-SRR coupling, despite the small number of electrons in the QD. The large coupling strength of the QD-SRR coupling can be explained by the strong electric field concentration near the QD by the side gate electrodes with sharp tips.

Our QD-SRR sample was fabricated by using a modulation-doped AlGaAs/GaAs high mobility heterojunction wafer (see Sec. I of Supplemental Material for the wafer property [25]). We measured two slightly different types of QDs, which were named samples A and B. The geometry of sample A is shown in Fig. 1(a) (refer to Sec. II of Supplemental Material for the geometry of sample B [25]). The SRR works as a subwavelength THz optical resonator that utilizes a concept of a lumped LC resonance circuit and has a shape of letter C, as shown on the left of the illustration [26]. By applying negative voltages to the two side gates and the SRR, the QD is formed between them as shown by a red circle in the left panel of Fig. 1(a). Further information on the experimental methods are explained in Appendix A.

Before going into further explanation of our experiments, we show here what is expected to be observed in this experiment. Since the 2D electrons are present in the vicinity of the SRR even when the 2DES below the

* kuroyama@iis.u-tokyo.ac.jp

† hirakawa@iis.u-tokyo.ac.jp

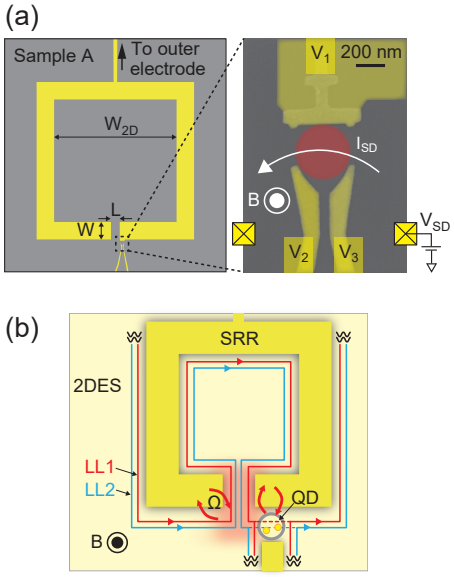

Fig. 1. (a) Left panel shows an illustration of our QD-SRR coupled sample. The gap length, L, was designed to be 1 μm. The right panel shows a scanning electron microscope image of the QD region. The black crosses represent AuGeNi ohmic contacts. (b) Illustration of the 2DES-SRR-QD coupled model system considered in this work. Red and blue lines pictorially represent the quantum Hall edge channels propagating along the SRR when the filling factor of the bulk region is assumed to be 2. "LL1" and "LL2" are the lowest and the second lowest Landau levels, respectively.

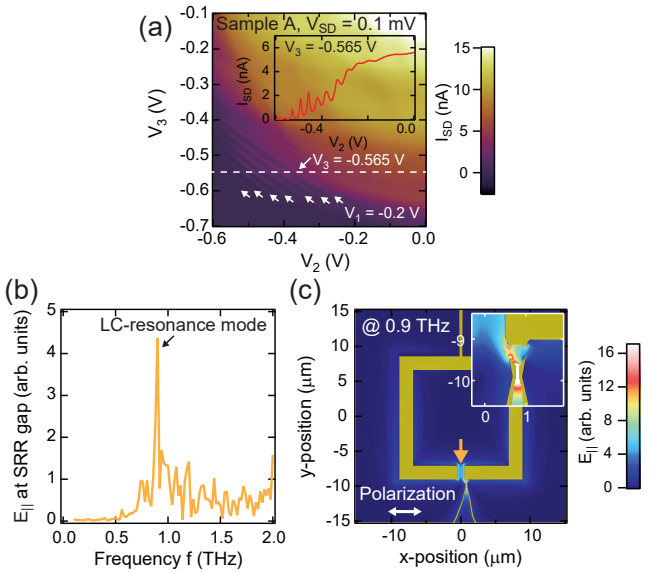

Fig. 2. (a) DC current through the QD measured at $V_{\rm SD} = 0.1$ mV as a function of the two side gate voltages. The current peaks indicated by white arrows are the Coulomb oscillation of the QD. The inset is the current measured through the QD as a function of V_2 along the white dashed line. (b) Spectrum of the in-plane electric field strength $E_{\parallel}$ in the SRR gap, calculated by the frequency-domain finite element method (FDFEM). (c) Numerically calculated intensity map of $E_{\parallel}$ of the incident radiation in the 2D electron layer plane ($\sim$ 100 nm below the surface) plotted at 0.9 THz. The inset is a magnified view around the QD location.

SRR is depleted by the negative gate voltages, it is reasonable to expect that not only the electrons in the QD but also the 2D electrons in the vicinity of the SRR are simultaneously coupled to the SRR. As explained later, 2D electrons in the quantum Hall edge channels propagating along the SRR mainly couple with the SRR [27]. This consideration is summarized in Fig. 1(b), where g and Ω denote the coupling strength between electrons in the QD and the SRR and that between the 2D electrons in the edge channels and the SRR, respectively. Thus, we expect to observe energy dispersions of the QD-SRR-2DES three-body coupled system in our experiments.

To characterize the electron transport through the QD without THz radiation, we measured the conductance at $B = 0$ as a function of V_2 and V_3 applied to the side gates when the 2D electrons beneath the SRR were depleted by applying V_1 to the SRR, as shown in Fig. 2(a). Coulomb oscillations are clearly observed (white arrows in the figure), indicating that a QD is formed at the designed position and the electron number can be precisely controlled.

Next, by using the frequency-domain finite element method (FDFEM), we calculated the spectrum of the in-plane electric field, $E_{\parallel} = \sqrt{|E_x|^2 + |E_y|^2}$, in the SRR gap region. Note that we took into account the actual structure of the metal electrodes but neglected the 2D electron layer. The calculated spectrum is shown in Fig. 2(b). The calculated resonance spectrum has a peak at 0.9 THz, which is the lowest excitation mode of the SRR (the LC-resonance mode). Figure 2(c) shows the spatial distribution of $E_{\parallel}$ at the resonance frequency in the plane 100-nm-deep from the surface. The electric field enhancement is clearly observed near the SRR gap (see an orange arrow) and is extended to the region where the QD is located, thanks to field focusing effect by the sharp side-gate electrodes.

As a reference experiment, we first measured photocurrent without forming a QD as a function of the B-field and the frequency of the incident THz radiation, f, as shown in Fig. 3(a), when $V_{\rm SD}$ was set to be zero. Note that, since we cooled down the sample, while applying +0.3 V to all the gate electrodes, +0.3 V corresponds to the nearly flat band condition [28]. The B-field-independent signals observed below 0.3 THz are induced by the lead, which is connected to the SRR for the sake of wire bonding (not shown in Fig. 1(a)) and works as an antenna for low frequency electromagnetic waves. The vertical modulation pattern that depends only on the B-field in the spectral map originates from the Shubnikov-de Haas (SdH) oscillation. A signal indicated by a blue arrow is the cyclotron resonance (CR) of the 2D electrons. Since the CR signal appears over a wide range be-

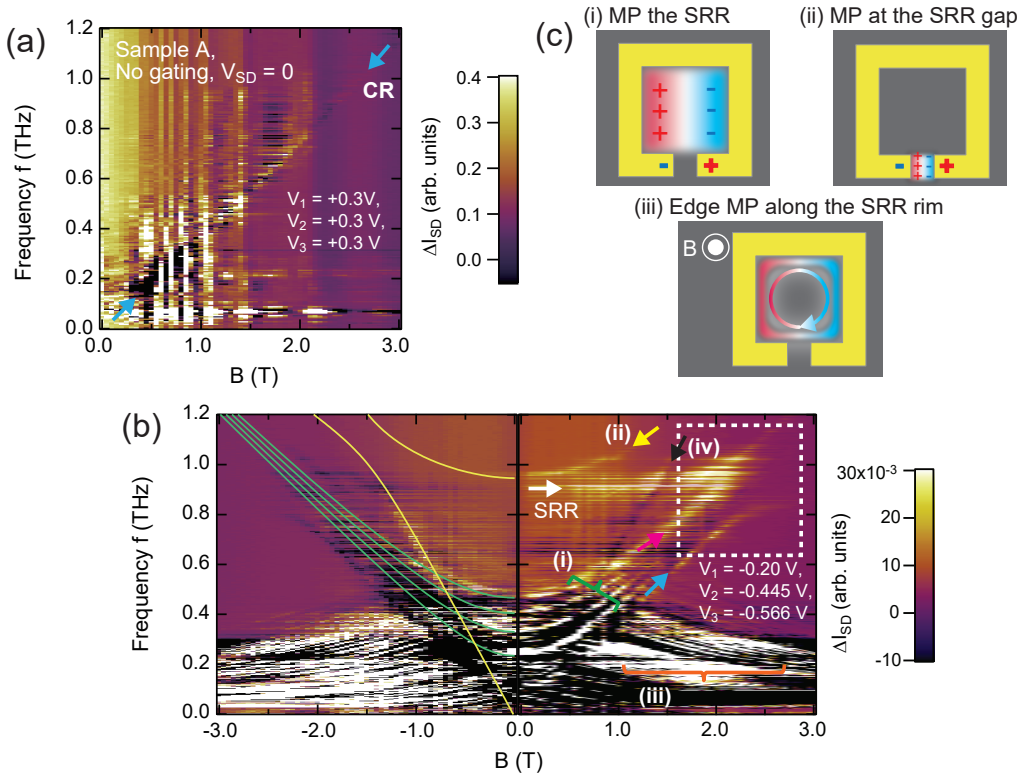

Fig. 3. (a) Color-coded map of the THz-induced photocurrent measured as a function of the incident THz frequency, f, and the external magnetic field, B, at $V_{\rm SD} = 0$, when V_1, V_2 and V_3 are set to the flatband condition (+0.3 V). The cyclotron resonance signal appears, as indicated by a blue arrow. (b) Color-coded map of the THz-induced photocurrent through the QD formed by applying negative gate voltages to V_1, V_2 and V_3. The photocurrent was measured at $V_{\rm SD} = 0$ as a function of f and B. The B-field independent signal at 0.9 THz is assigned to the resonant absorption by the SRR. The signal which appears above $B = 1.5$ T (indicated by a blue arrow) shows an anti-crossing against the SRR resonant absorption. The numbers (i)-(iii) respectively correspond to the magnetoplasmon modes illustrated in Fig. 3(c). The second harmonic of the cyclotron excitation is indicated by a black arrow. Energy dispersions of the plasmonic excitations in the interior of the SRR (green curves) and those of the coupled states between the plasmonic excitation in the SRR gap and the second harmonic of the cyclotron excitation (yellow curves) are fitted to the observed photocurrent map. (c) Pictorial explanations for the magnetoplasmon (MP) modes excited in the 2D electron system surrounded by the SRR.

tween the SdH peaks, the cyclotron excitations observed in the photocurrent are likely to take place in the quantum Hall edge channels [29].

Next, we measured the photocurrent spectrum with the QD formed by applying voltages to the finger gates, V_2 and V_3. Figure 3(b) shows a color-coded photocurrent map measured at the QD source-drain bias voltage $V_{\rm SD} = 0$ as a function of B and f (the same colormap without eye guides is plotted in Fig. S3(a) of Supplemental Material [25]). The signal located at around 0.9 THz is assigned to the resonant absorption of the SRR, as expected from Fig. 2(b). Note that several other signals which depend on the B-field are observed, as labeled (i) to (iv) in Fig. 3(b), suggesting that they originate from electronic excitations in the system (see Appendix B for the explanations). Although these electronic excitations are very intriguing, we will not go into more detail. Here, we focus ourselves on the fact that the conductance peak indicated by a blue arrow shows an anti-crossing behavior when it approaches the SRR resonance frequency. The observed anti-crossing indicates that the 2D electrons are coherently coupled with the SRR.

The photocurrent signal indicated by a blue arrow in Fig. 3(b) can be attributed to the CR of the 2D electrons. Note that the observed signal changes its polarity when the B-field direction is reversed, indicating that the signal originate from the Hall conductance of the 2D electrons. Therefore, electrons in the chiral quantum Hall edge states propagating near the SRR, which are illustrated by blue and red lines in Fig. 1(b) for the case of the filling factor $\nu = 2$ (the spin degeneracy neglected), are very likely to create the anti-crossing with the SRR. Note that "LL1" and "LL2" in Fig. 1(b) denote the lowest and the second lowest Landau levels, respectively. In addition, the photocurrent signal indicated by a magenta arrow in Fig. 3(b) appears from the B-field similar to the CR of the 2D electrons. As we discuss in Appendix C, since the signal appears only when the electrical con-

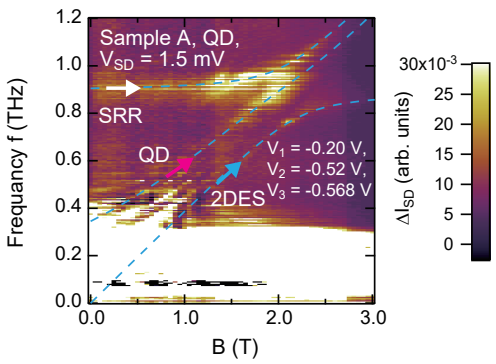

Fig. 4. Calculated energy dispersions of the 2DES-SRR-QD coupled system (blue dashed lines) are plotted on the color-coded map of the THz-induced photocurrent through the QD, measured at $V_{\rm SD} = 1.5$ mV.

striction between the side gate electrode and the SRR is strong, as when the QD formed in the present experiment, it can be attributed to the resonant excitation of electrons in the QD.

So far, we have made assignments of the various photocurrent signals observed in Fig. 3(b) (see Appendices B and C). In the following, we want to focus ourselves on the anti-crossing behavior in the photocurrent signals enclosed by a white dashed rectangle in Fig. 3(b), which can be explained by the simultaneous coupling of 2D electrons, electrons in the QD, and the SRR. Electrons confined in the QD as well as 2D electrons near the SRR gap can interact with the SRR, because the THz field is strongly enhanced (as shown in Fig. 2(c)). We calculate the energy dispersions of the 2DES-SRR-QD coupled system whose Hamiltonian describes the excitations of $|e_{\rm 2DES}\rangle$; $|g_{\rm 2DES}, n = 1, g_{\rm QD}\rangle$; $|g_{\rm 2DES}, n = 0, e_{\rm QD}\rangle$), where g_i and e_i (i =2DES,QD) are the ground and excited states of the 2DES and QD, and n is the photon number in the SRR;

$$\mathcal{H} = \hbar \begin{pmatrix} \omega_c(B) & \Omega(B) & 0 \\ \Omega(B) & \omega_{\rm SRR} & g(B) \\ 0 & g(B) & \omega_{\rm QD}(B) \end{pmatrix}. \qquad (1)$$

Note that we do not take into account the squared terms of the vector potential and the counter-rotating terms of the dipolar interaction. Also, we did not consider the interaction between the 2D electrons and electrons in the QD in this model. Here, $\omega_c = eB/m^*$ is the CR frequency and we used $m^* = 0.071m_0$ as the electron effective mass in GaAs. $\omega_{\rm QD} = \sqrt{\omega_0^2 + (\omega_c/2)^2} + \omega_c/2$ is the excitation frequency of electrons in the QD [30, 31]. $\hbar\omega_0$ is the QD orbital spacing energy at $B = 0$. g is the Rabi frequency between the electrons in the QD and the SRR. Similarly, Ω is the Rabi frequency between the 2DES and the SRR. Their B-field dependences are $g \simeq g_0\sqrt{B/B_{\rm resQD}}$ obtained from the Fock-Darwin wavefunctions and $\Omega = \Omega_0\sqrt{B/B_{\rm res2DES}}$, where $B_{\rm resQD}$ and $B_{\rm res2DES}$ are defined by $\omega_{\rm QD}(B_{\rm resQD}) = \omega_{\rm SRR}$, and $\omega_c(B_{\rm res2DES}) = \omega_{\rm SRR}$ [32, 33]. We derived the polariton energies by diagonalizing the Hamiltonian matrix. The photocurrent map in Fig. 4 was measured at $V_{\rm SD} = 1.5$ mV and at a gate voltage slightly different from that for Fig. 3(b) (the same colormap without eye guides is plotted in Fig. S3(b) of Supplemental Material [25]). The fitted energy dispersion curves with $\omega_{\rm SRR}/2\pi = 905$ GHz, $\omega_0/2\pi = 345$ GHz, $\Omega_0/2\pi = 100$ GHz, and $g_0/2\pi = 50$ GHz are shown in Fig. 4 by blue dashed lines. The calculated lines reproduce the spectral features very well, indicating that the signal marked with a magenta arrow can be attributed to the electron excitation in the QD. From this analysis, $\Omega_0/\omega_{\rm SRR}$ is as large as 0.1, meaning that the 2DES-SRR coupled system is in the ultrastrong coupling regime. Furthermore, the QD-SRR coupling is also remarkably large, despite the fact that the QD accommodates only a few electrons.

In recent works, large coupling constants between 2D electrons and SRRs were realized by utilizing collective excitations of AlGaAs/GaAs 2D electron systems of high carrier densities or of multiple electron layers to enhance the coupling strength. In this sense, we are going in the opposite direction, since the QD is operated in a few-electron regime. To examine whether even a single electron in a QD can have a large coupling strength, we have made a simple estimation of coupling strength between a single electron dipole in a QD and the SRR. The electric field created by a single photon of an energy $\hbar\omega_{\rm SRR}$ in the SRR gap is expressed as $E_{\rm gap} \simeq \sqrt{\hbar\omega_{\rm SRR}/\epsilon\epsilon_0 WL^2}$, where $\epsilon = 4.57$ is the effective dielectric constant for an GaAs-vacuum interface, which is estimated from the magnetoplasmon energy dispersion (see Appendix B for the explanation). Note that the mode volume at the QD location is ignored because its contribution to the total mode volume of the SRR is small. For simplicity, we assumed that the electric field extends perpendicular to the SRR by a distance $\simeq L$ [34]. Note that, according to the numerical calculation shown in Fig. 2(c), the electric field around the QD position is 4 times larger than that in the SRR gap region, because the electric field is concentrated in the small gap between the sharp finger gates and the SRR. The QD confinement length of a single electron in the QD under perpendicular B-field is described as $l = l_B[1/4 + (\omega_c/\omega_{\rm QD})^2]^{1/4}$, where $l_B = \sqrt{\hbar/eB}$ is the magnetic length. Since the QD-SRR coupling is realized by the electric-dipole interaction, the Rabi frequency of a single electron in the QD is calculated as $g_0 \simeq el(4E_{\rm gap})/\hbar$. Using this relationship for our sample geometry at $B_{\rm resQD} \sim 1.96$ T, the Rabi frequency for a single electron and a single photon is calculated to be $g_0/2\pi \sim 58.9$ GHz, which is close to the experimentally estimated g_0. We can trace the origin of the very strong coupling between a single electron in the QD and the SRR back to a large enhancement in the electric field due to field enhancement by the sharp tips of the finger gates.

In conclusion, we have investigated THz-induced photocurrent through the QD in the 2DES-SRR-QD cou-

pled system. We have observed a remarkably large anticrossings generated by the coupling between the SRR and electronic excitations in the QD as well as 2DES. The calculated energy dispersion of the 2DES-SRR-QD polaritonic states is in good agreement with the observed THz photocurrent spectrum. The normalized coupling strength $\Omega_0/\omega_{\rm SRR}$ is as large as 0.1, indicating that the 2DES-SRR coupled system is in the ultrastrong coupling regime. The B-field polarity dependence of the photocurrent signal indicates that the 2D electrons that strongly interact with the SRR lie in the quantum Hall edge states along the edge of the SRR. Furthermore, the electronic excitations in the QD also exhibit coherent coupling with the SRR with a remarkably large coupling constant, thanks to the strong enhancement of THz electric fields by the sharp tips of the finger gates.

The present lithography-defined coupled system allows us to investigate quantum transport of polaritons by using simple transport measurements. These studies greatly benefit the understanding of fundamental physics of polaritons and their manybody effects in the polaritonic quantum phase transition [35–37]. Furthermore, owing to its simple design, the present QD-SRR hybrid system is suitable for larger system integration. By improving the shape and geometry of the QD finger gates, it may be possible that the coupling strength of the QD-SRR system reaches the ultrastrong light-matter coupling regime.

We thank S. Komiyama, S. Iwamoto, Y. Tokura, S. Mikhailov, and S. Q. Du for fruitful discussions. This work has been supported by JSPS Research Fellowship for Young Scientists (JP19J01737), and KAKENHI from JSPS (JP20K14384, JP20H05660, JP17H01038, JP15H05868, JP17H06119, JP20K15260, JP20H05218, and JP15H05700)), and JST, PRESTO Grant Number JPMJPR2255, Japan.

Appendix A: Appendix on the experimental methods

We describe details of the QD-SRR hybrid sample and the THz optical setup. The two side gates and the SRR shown in Fig. 1(a) were formed by depositing a Ti/Au layer. The size of our SRR (the outer rim) was 18×18 μm^2. The gap width, W, and length, L, were designed to be 2 μm and 1 μm, respectively. By fitting a Lorentzian function to the SRR absorption peak in Fig. 3(b), the quality (Q)-factor of the SRR is estimated to be 13, corresponding to the full width at half maximum (FWHM) of about 68 GHz, which is similar to the one reported in the previous studies [18, 23]. The QD was formed very near the gap of the SRR by applying appropriate negative voltages to V_1 and the two side gates, V_2 and V_3. Note that 2D electrons beneath the SRR are depleted, while those in the interior of the SRR ring and in the gap region remain. The source-drain bias voltage, $V_{\rm SD}$, was applied across the QD through the ohmic contacts illustrated by black crosses in Fig. 1(a). All the measurements were performed at the base temperature ($\sim$ 0.32 K) of a ^{3}He cryostat (the entire setup is illustrated in Fig. S1 in Supplemental Material). The sample was attached on a Si hemispherical lens to focus the incident monochromatic THz radiation onto the samples from the substrate side. Monochromatic THz radiation was generated by the difference frequency generation, using two frequency-tunable laser diodes together with a uni-traveling carrier photodiode (UTC-PD). The output frequency can be tuned from 0.1 to 3 THz. The THz output power is approximately 1 μW at around 0.1 THz and decreases to 100 pW at 3 THz. The output power of the UTC-PD was periodically modulated at 83 Hz. We measured the THz-induced photocurrent through the QD.

Appendix B: Appendix on the other electronic excitations observed in Fig. 3(b)

Since the electron transport through a QD is sensitive to its electromagnetic environment, the measured QD conductance shown in Fig. 3(b) reflects various kinds of electronic excitations in the system as indicated by numbers (i)-(iv). Here, we discuss the origin of the THz-induced signals.

(i) The signals indicated in green, which shift to higher frequencies with increasing B, are assigned to the magnetoplasmon excitations of electrons inside the ring of the SRR (see (i) of Fig. 3(c)). Similar magnetoplasmon excitations were observed in absorption experiments performed in the gigahertz and THz frequency ranges [38, 39]. The energies of magnetoplasmons can be calculated by the following formula.

$$\omega_{{\rm p},N} = \sqrt{\frac{\pi N n_{\rm 2D} e^2}{2m^* \epsilon \epsilon_0 W_{\rm 2D}}} \tag{B1}$$

where $n_{\rm 2D}$ is the 2D electron density, and $W_{\rm 2D}$ is the width of the 2D electron system (2DES) that remains in the interior of the SRR. ϵ is the effective dielectric constant for the interface between GaAs and vacuum. N is the harmonic number of the magnetoplasmon modes. Under a B-field, the magnetoplasmon energy is expressed as,

$$\omega_{{\rm MP},N} = \sqrt{\omega_{{\rm p},N}^2 + \omega_c^2}. \tag{B2}$$

The plasmon dispersions calculated for $N = 1 \sim 4$ and $W_{\rm 2D}$ = 14 μm, and ϵ = 4.57 are plotted by green curves and are in good agreement with the observed signals, as shown in the left figure of Fig. 3 (b) of the main text. Note that the effective dielectric constant is smaller than that expected for the GaAs-vacuum interface. This discrepancy may be due to the fact that the 2D electrons are

surrounded by the metal electrodes. In addition, according to previous theoretical studies [40, 41], a uniform incident electromagnetic field can excite only odd-order magnetoplasmons in a spatially uniform 2DES. Therefore, observation of the even-order magnetoplasmons suggests that incident THz may be non-uniform. Details will be discussed elsewhere.

(ii) Magnetoplasmon excitation of 2D electrons that remain in the gap region of the SRR (see the middle illustration (ii) of Fig. 3(c)) is observed slightly above the resonance frequency of the SRR (see a yellow arrow in Fig. 3(b)).

(iii) The signals showing red shifts with increasing B are also observed (orange curly bracket in Fig. 3(b)). These excitations are explained by circulating motion of magnetoplasmons propagating along the inner edge of the SRR (see illustration (iii) of Fig. 3(c)). Because the propagating orientation of the edge magnetoplasmon along the inner edge is opposite to that of the cyclotron motions, the resonance frequency decreases with B. Their energy spacing is approximately 10 GHz, which is much smaller than that of the magnetoplasmon modes discussed above. A similar energy dispersion of the magnetoplasmon excitation was observed in a 2DES of a rectangle shape [42] and explained by the edge magnetoplasmon excitation. However, unlike the previous study [42], many higher order harmonic excitations appear in our spectrum, which calls for future study.

(iv) We also note that the second harmonic of the cyclotron resonance (CR) is clearly observed, which is forbidden for a uniform 2DES by the optical selection rule under the long-wavelength approximation (see a black arrow in Fig. 3(b)). It has been known that this second harmonic mode can be excited when an electric field has a spatial nonuniformity [43–45]. In this condition, the long-wave approximation breaks down, and the excitation of higher-order harmonics of CR becomes allowed in the SRR gap. The detailed discussion will be reported in our future publication.

We make a further comment on (ii) the magentplasmon excitation in the SRR gap and (iv) the second harmonic of the CR. We fit the signals by the following energy dispersions of the coupled states obtained by the Jaynes-Cummings model.

$$\omega^{\pm}_{\mathrm{2CR-MP}}(B) = \frac{\omega_{\mathrm{2CR}} + \omega_{\mathrm{MP}}}{2} \pm \frac{\sqrt{(\omega^2_{\mathrm{MP}} - \omega_{\mathrm{2CR}})^2 + 4\Omega^2_{\mathrm{2CR}}}}{2}, \quad \text{(B3)}$$

where

$$\omega_{\mathrm{2CR}} = \frac{2eB}{m^*_{\mathrm{2CR}}}. \quad \text{(B4)}$$

m^*_{2CR} is the effective mass for the second harmonic of the CR. Ω_{BS} is the coupling strength between the magnetoplasmon excitation and the second harmonic of the CR. The energy dispersions are calculated by using $m^*_{\mathrm{2CR}} = 0.076m_0$, $\omega_{\mathrm{p}} = 935$ GHz, and $\Omega_{\mathrm{2CR}} = 100$ GHz. The result is plotted by yellow curves in Fig. 3(b) in the main text and can fit the obtained photocurrent spectrum. Note that m^*_{2CR} is larger than the effective mass used for the calculation of other electronic excitations. According to Eq. (B1), the length of the 2DES in the SRR gap region was estimated to be 0.9 μm, which is consistent with the geometrical gap of the SRR (1 μm).

As explained above, we have observed various kinds of magnetoplasmon excitations of 2D electrons by the photocurrent spectroscopy of the QD. They are indeed interesting but are not in the scope of the present paper. Therefore, we will not go into detail and discuss them in future publications.

Appendix C: Appendix on the resonant excitation of the QD observed in the photocurrent spectra

In order to interpret the signal indicated by a magenta arrow in Fig. 3(b), we compared photocurrent spectra measured when a QD is formed near the SRR and when a QD is not formed. Fig. 5(a) shows a color-coded map of photocurrent through a QPC measured a function of B and f on sample B. Note that, since the flat-band is achieved when the gate voltages are set to be +0.3 V, even $V_1 = 0$ works as a negative bias. An anti-crossing signal between the 2D electrons and the SRR is observed in the range B = 2-3 T. Since we applied small voltages to V_1 and V_2, the electrostatic constriction in the QPC is very weak. In this condition, only the anticrossing signal between the CR of the 2D electrons and the SRR (dark purple region in Fig. 5(a)) and the 2D magnetoplasmon excitation in the interior of the SRR are observed. Fig. 5(b) exhibits a color-coded map of a photocurrent measured when a QD is formed near the SRR by applying more negative voltage on the SRR and the side gates. In contrast to Fig. 5(a), one more spectral line indicated by a magenta arrow appears between the resonance mode of the SRR and the CR of the 2D electrons, which is similar to the photocurrent spectrum shown in Fig. 3(b). Since this signal is observed only when the QD is formed near the SRR, we can conclude that this line originates from the resonant excitation in the QD.

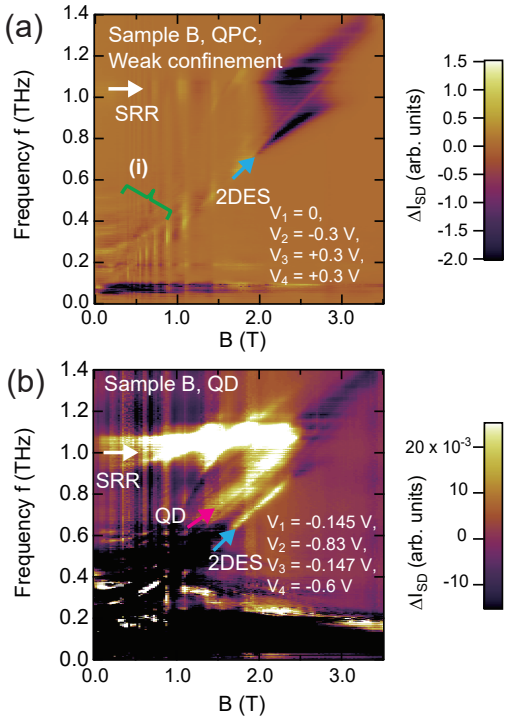

Fig. 5. (a) Color-coded map of the THz-induced photocurrent measured as a function of the incident THz frequency, f, and the external magnetic field, B, at $V_{SD} = 0$, measured when a weakly constricted QPC is formed (sample B). (b) Color-coded map of the THz-induced photocurrent through the QD measured as a function of f and B, measured on the same sample. A new line appears in-between the original anti-crossing gap, similar to that in Fig. 3(b) (see a magenta arrow).

[1] R. Hanson, L. P. Kouwenhoven, J. R. Petta, S. Tarucha, and L. M. K. Vandersypen, Rev. Mod. Phys. **79**, 1217 (2007).

[2] P. Stano and D. Loss, Nature Reviews Physics **4**, 672 (2022).

[3] G. Burkard, T. D. Ladd, A. Pan, J. M. Nichol, and J. R. Petta, Rev. Mod. Phys. **95**, 025003 (2023).

[4] K. Kuroyama, M. Larsson, S. Matsuo, T. Fujita, S. R. Valentin, A. Ludwig, A. D. Wieck, A. Oiwa, and S. Tarucha, Scientific Reports **7**, 16968 (2017).

[5] K. Kuroyama, M. Larsson, C. Y. Chang, J. Muramoto, K. Heya, T. Fujita, G. Allison, S. R. Valentin, A. Ludwig, A. D. Wieck, S. Matsuo, A. Oiwa, and S. Tarucha, Phys. Rev. B **99**, 085203 (2019).

[6] T. Fujita, K. Morimoto, H. Kiyama, G. Allison, M. Larsson, A. Ludwig, S. R. Valentin, A. D. Wieck, A. Oiwa, and S. Tarucha, Nature Communications **10**, 2991 (2019).

[7] T. Yoshie, A. Scherer, J. Hendrickson, G. Khitrova, H. M. Gibbs, G. Rupper, C. Ell, O. B. Shchekin, and D. G. Deppe, Nature **432**, 200 (2004).

[8] J. P. Reithmaier, G. Sek, A. Löffler, C. Hofmann, S. Kuhn, S. Reitzenstein, L. V. Keldysh, V. D. Kulakovskii, T. L. Reinecke, and A. Forchel, Nature **432**, 197 (2004).

[9] E. Peter, P. Senellart, D. Martrou, A. Lemaître, J. Hours, J. M. Gérard, and J. Bloch, Phys. Rev. Lett. **95**, 067401 (2005).

[10] K. Hennessy, A. Badolato, M. Winger, D. Gerace, M. Atatüre, S. Gulde, S. Fält, E. L. Hu, and A. Imamoğlu, Nature **445**, 896 (2007).

[11] K. D. Petersson, L. W. McFaul, M. D. Schroer, M. Jung, J. M. Taylor, A. A. Houck, and J. R. Petta, Nature **490**, 380 (2012).

[12] X. Mi, J. V. Cady, D. M. Zajac, P. W. Deelman, and J. R. Petta, Science **355**, 156 (2017).

[13] A. J. Landig, J. V. Koski, P. Scarlino, U. C. Mendes, A. Blais, C. Reichl, W. Wegscheider, A. Wallraff, K. Ensslin, and T. Ihn, Nature **560**, 179 (2018).

[14] P. Scarlino, J. H. Ungerer, D. J. van Woerkom, M. Mancini, P. Stano, C. Müller, A. J. Landig, J. V. Koski, C. Reichl, W. Wegscheider, T. Ihn, K. Ensslin, and A. Wallraff, Phys. Rev. X **12**, 031004 (2022).

[15] P. Harvey-Collard, J. Dijkema, G. Zheng, A. Sammak, G. Scappucci, and L. M. K. Vandersypen, Phys. Rev. X **12**, 021026 (2022).

[16] Y. Todorov, A. M. Andrews, R. Colombelli, S. De Liberato, C. Ciuti, P. Klang, G. Strasser, and C. Sirtori, Phys. Rev. Lett. **105**, 196402 (2010).

[17] G. Scalari, C. Maissen, D. Turčinková, D. Hagenmüller, S. D. Liberato, C. Ciuti, C. Reichl, D. Schuh, W. Wegscheider, M. Beck, and J. Faist, Science **335**, 1323 (2012).

[18] G. L. Paravicini-Bagliani, F. Appugliese, E. Richter, F. Valmorra, J. Keller, M. Beck, N. Bartolo, C. Rössler, T. Ihn, K. Ensslin, C. Ciuti, G. Scalari, and J. Faist, Nature Physics **15**, 186 (2019).

[19] M. Jeannin, G. Mariotti Nesurini, S. Suffit, D. Gacemi, A. Vasanelli, L. Li, A. G. Davies, E. Linfield, C. Sirtori, and Y. Todorov, ACS Photonics **6**, 1207 (2019).

[20] M. Jeannin, T. Bonazzi, D. Gacemi, A. Vasanelli, L. Li, A. G. Davies, E. Linfield, C. Sirtori, and Y. Todorov, Nano Letters **20**, 4430 (2020).

[21] E. Mavrona, S. Rajabali, F. Appugliese, J. Andberger, M. Beck, G. Scalari, and J. Faist, ACS Photonics **8**, 2692 (2021).

[22] F. Appugliese, J. Enkner, G. L. Paravicini-Bagliani, M. Beck, C. Reichl, W. Wegscheider, G. Scalari, C. Ciuti, and J. Faist, Science **375**, 1030 (2022).

[23] S. Rajabali, S. Markmann, E. Jöchl, M. Beck, C. A. Lehner, W. Wegscheider, J. Faist, and G. Scalari, Nature Communications **13**, 2528 (2022).

[24] F. Valmorra, K. Yoshida, L. C. Contamin, S. Messelot, S. Massabeau, M. R. Delbecq, M. C. Dartiailh, M. M. Desjardins, T. Cubaynes, Z. Leghtas, K. Hirakawa, J. Tignon, S. Dhillon, S. Balibar, J. Mangeney, A. Cottet, and T. Kontos, Nature Communications **12**, 5490 (2021).

[25] See Supplemental Material at [url] for the basic properties of the GaAs-based heterojunction wafer (Section I), the geometry sample B (Section II). In addition, Fig. S1 shows the optical setup for THz spectroscopy on the QD-SRR coupled sample, and Figs. S3(a) and S3(b) show Figs. 3(b) and 5 without eye guides and arrows, respectively.

[26] D. R. Smith, W. J. Padilla, D. C. Vier, S. C. Nemat-Nasser, and S. Schultz, Phys. Rev. Lett. **84**, 4184 (2000).

[27] K. Kuroyama, J. Kwoen, Y. Arakawa, and K. Hirakawa, Nano Letters 10.1021/acs.nanolett.3c02272 (2023).

[28] C. Buizert, F. H. L. Koppens, M. Pioro-Ladrière, H.-P. Tranitz, I. T. Vink, S. Tarucha, W. Wegscheider, and L. M. K. Vandersypen, Phys. Rev. Lett. **101**, 226603 (2008).
[29] K. Hirakawa, K. Yamanaka, Y. Kawaguchi, M. Endo, M. Saeki, and S. Komiyama, Phys. Rev. B **63**, 085320 (2001).
[30] V. Fock, Zeitschrift für Physik **47**, 446 (1928).
[31] C. G. Darwin, Mathematical Proceedings of the Cambridge Philosophical Society **27**, 86–90 (1931).
[32] N. Bartolo and C. Ciuti, Phys. Rev. B **98**, 205301 (2018).
[33] C. Ciuti, Phys. Rev. B **104**, 155307 (2021).
[34] G. L. Paravicini-Bagliani, G. Scalari, F. Valmorra, J. Keller, C. Maissen, M. Beck, and J. Faist, Phys. Rev. B **95**, 205304 (2017).
[35] Y. Ashida, A. İmamoğlu, J. Faist, D. Jaksch, A. Cavalleri, and E. Demler, Phys. Rev. X **10**, 041027 (2020).
[36] Y. Todorov and C. Sirtori, Phys. Rev. X **4**, 041031 (2014).
[37] F. Schlawin, A. Cavalleri, and D. Jaksch, Phys. Rev. Lett. **122**, 133602 (2019).
[38] I. Grigelionis, M. Bialek, M. Grynberg, M. Czapkiewicz, V. Kolkovskiy, M. Wiater, T. Wojciechowski, J. Wróbel, T. Wojtowicz, D. BUT, W. Knap, and J. Lusakowski, Acta Physica Polonica A **122**, 1069 (2012).
[39] Y. Yu, Z. Zheng, H. Qin, J. Sun, Y. Huang, X. Li, Z. Zhang, D. Wu, Y. Cai, B. Zhang, and V. V. Popov, Opt. Express **26**, 31794 (2018).
[40] S. A. Mikhailov and N. A. Savostianova, Phys. Rev. B **71**, 035320 (2005).
[41] S. A. Mikhailov and N. A. Savostianova, Phys. Rev. B **74**, 045325 (2006).
[42] D. B. Mast, A. J. Dahm, and A. L. Fetter, Phys. Rev. Lett. **54**, 1706 (1985).
[43] A. V. Chaplik and D. Heitmann, Journal of Physics C: Solid State Physics **18**, 3357 (1985).
[44] E. Batke, D. Heitmann, and C. W. Tu, Phys. Rev. B **34**, 6951 (1986).
[45] S. Holland, C. Heyn, D. Heitmann, E. Batke, R. Hey, K. J. Friedland, and C.-M. Hu, Phys. Rev. Lett. **93**, 186804 (2004).